

Probing long-range structural order in SnPc/Ag(111) by umklapp process assisted low-energy angle-resolved photoelectron spectroscopy

Stephan Jauernik,^{*} Petra Hein, Max Gurgel, Julian Falke, and Michael Bauer*Institut für Experimentelle und Angewandte Physik, Christian-Albrechts-Universität zu Kiel, D-24098 Kiel, Germany*
 (Received 22 November 2017; revised manuscript received 16 February 2018; published 12 March 2018)

Laser-based angle-resolved photoelectron spectroscopy is performed on tin-phthalocyanine (SnPc) adsorbed on silver Ag(111). Upon adsorption of SnPc, strongly dispersing bands are observed which are identified as secondary Mahan cones formed by surface umklapp processes acting on photoelectrons from the silver substrate as they transit through the ordered adsorbate layer. We show that the photoemission data carry quantitative structural information on the adsorbate layer similar to what can be obtained from a conventional low-energy electron diffraction (LEED) study. More specifically, we compare photoemission data and LEED data probing an incommensurate-to-commensurate structural phase transition of the adsorbate layer. Based on our results we propose that Mahan-cone spectroscopy operated in a pump-probe configuration can be used in the future to probe structural dynamics at surfaces with a temporal resolution in the sub-100-fs regime.

DOI: [10.1103/PhysRevB.97.125413](https://doi.org/10.1103/PhysRevB.97.125413)

I. INTRODUCTION

The relevance of surface umklapp processes in photoemission has been emphasized in numerous studies [1–8]. These types of processes can provide information on a part of the bulk electronic structure which is otherwise hidden beyond the photoemission horizon [3]. Additionally, the umklapp processes intrinsically imprint information on the long-range order of the surface layer onto the photoemission signal and can, therefore, potentially complement other surface sensitive diffraction techniques such as low-energy electron diffraction (LEED) and x-ray photoelectron diffraction [2]. Also, the presence of a periodic bulk lattice can substantially affect the photoemission process, particularly at low excitation energies, as excitation channels in the valence electronic structure that are forbidden in a free-space scenario can open up [9]. In the photoemission spectrum these photoexcitation pathways appear as so-called primary Mahan cones or, if modified by a surface umklapp process, secondary Mahan cones [10]. Recently, the formation of Mahan cones has attracted some interest, partly due to the increased application of laser-based near-ultraviolet harmonic sources in photoemission experiments [11,12]. The most prominent example of a primary Mahan cone is a resonant *sp*-intra-band transition observed in low-energy photoemission experiments on silver and copper [13–15]. Secondary Mahan cones have been observed, for instance, after adsorption of a monolayer of Zn-phthalocyanine on Ag(110) [4] and for a Bi-covered Cu(111) surface [5]. Notably, these types of experiments are often performed using pulsed femtosecond laser sources potentially offering the capability of studying ultrafast structural processes on the ultimate time scales intrinsic to the lattice degrees of freedom.

In the present work we present an angle-resolved photoelectron spectroscopy (ARPES) study of SnPc adsorbed

on Ag(111) using the fourth harmonic of the near-infrared output of a femtosecond laser system. Past studies reported a complex structural phase diagram of the SnPc overlayer, which is schematically illustrated in Fig. 1(a). At low coverages the overlayer forms a disordered gas phase, whereas at coverages close to a monolayer (ML) a low-temperature commensurate phase (C-phase) and a high-temperature incommensurate phase (I-phase) are observed [16]. In the latter case repulsive interaction among the molecules results in a continuous adjustment of the overlayer structure as the coverage is increased. The system attracted additionally interest owing to the nonplanar geometry of SnPc [see Fig. 1(b)] [17], resulting in conformationally different adsorption geometries of the molecules [18,19]. It was shown that a controlled transformation (switching) of individual molecules from the tin-up to the tin-down configuration is possible by local electron or hole injection using an STM tip [20].

The ARPES data presented in this work show a multitude of strongly dispersing bands in the commensurate as well as in the incommensurate phase that are absent from the pristine

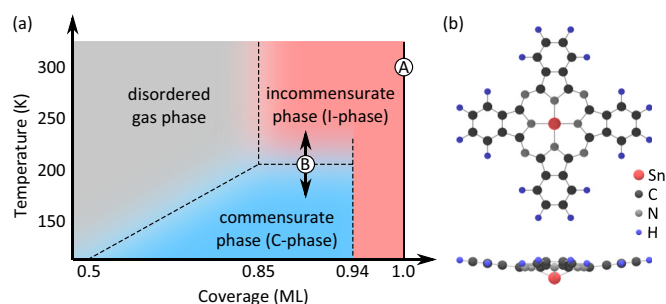


FIG. 1. (a) Structural phase diagram of SnPc/Ag(111) as a function of the temperature and coverage in the submonolayer regime; point A and path B mark the coverages and temperatures for which LEED and PES measurements were performed in the present study. (b) Molecular structure of SnPc: top view and side view.

^{*}jauernik@physik.uni-kiel.de

Ag(111) surface. Based on a comparison with simulations describing the Ag valence electronic structure in a nearly free electron approximation, we are able to assign these features to cuts through specific secondary Mahan cones resulting from the diffraction of photoexcited electrons in the bulk as they transit the ordered adsorbate layer. The temperature dependence of the ARPES signal is affected by thermally activated vibrational motion of the SnPc molecules and, furthermore, allows monitoring of the first-order phase transition from the incommensurate to the commensurate phase. In fact, we show that the quality of the low-energy photoelectron diffraction data is competitive with that of diffraction data recorded in a conventional LEED configuration. As the present photoemission study was conducted with femtosecond laser pulses we envision that in a pump-probe configuration the spectroscopy of Mahan cones will in the future enable one to probe structural dynamics of surfaces with unprecedented time resolution, providing at the same time information on the nonequilibrium dynamics of potentially involved photoexcited carriers. By this means time-resolved Mahan-cone spectroscopy can complement other time-resolved electron diffraction techniques, which are often intrinsically limited in their time resolution by space charge broadening due to Coulomb interaction among the probing electrons [21,22].

II. EXPERIMENT

A scheme of the experimental setup, consisting of a tunable femtosecond laser system and an ultrahigh vacuum chamber, is shown in Fig. 2(a). Sub-50-fs laser pulses are delivered from two noncollinear optical parametric amplifiers (NOPAs; Orpheus-N-2H and -N-3H; Light Conversion) which are pumped by the second and third harmonics of a chirped pulsed amplifier (Pharos; TOPAG; 1030 nm, 220 fs, 500 kHz), respectively. The system output can be tuned continuously over a wavelength range from 500 to 950 nm (Orpheus-N-3H) and from 650 to 900 nm (Orpheus-N-2H). Internal second harmonic generation stages in both NOPA systems (SH output) allow extending this range up to 250 nm. Pulse energies and durations as a function of the wavelength as delivered by the laser system are shown in Fig. 2(b). ARPES spectra presented in this work were recorded at a wavelength of 210 nm (5.9 eV) generated by external frequency doubling of the 420-nm second harmonic output of one of the NOPA systems. The polarization of the laser light was adjusted with a zero-order $\lambda/2$ -wave plate. As shown in Fig. 2(a), the optical setup is prepared for performing time-resolved bichromatic experiments by independently combining the various outputs of the two NOPAs.

Photoelectrons are collected using a hemispherical energy analyzer (Phoibos 100; SPECS) which allows for simultaneous detection of the kinetic energy and the emission angle of electrons emitted from the sample onto a plane determined by the orientation of the analyzer entrance slit. More specifically, the experiments presented here were performed in a geometry as illustrated in Fig. 2(c), with the sample surface normal being aligned parallel to the analyzer lens axis. Azimuthal rotation of the sample allowed access to the high-symmetry directions $\bar{K}-\bar{\Gamma}-\bar{K}$ and $\bar{M}(X)-\bar{\Gamma}-\bar{M}(L)$ of the Ag(111) surface. The energy and angular resolution of the analyzer used in this

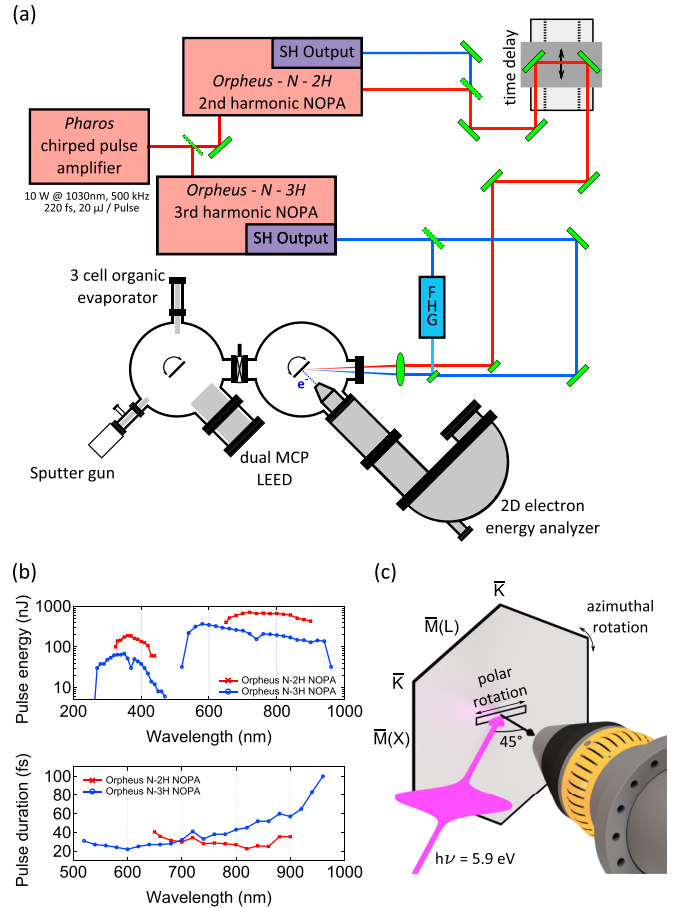


FIG. 2. (a) Scheme of the laser-based ARPES setup prepared for performing time-resolved experiments; laser-light is provided by two independent NOPA systems which are pumped by a chirped pulse amplifier. For the experiments presented here 210-nm light was used generated in a fourth harmonic generation unit (FHG). Photoelectrons are analyzed using a hemispherical 2D electron energy analyzer for simultaneous detection of the energy and momentum. The ultrahigh vacuum system is additionally equipped with a LEED unit and a standard surface preparation chamber. (b) Key specifications of the laser system: pulse energy and pulse duration of the fundamental and second harmonic output of the two NOPA systems. (c) Schematic of the ARPES geometry in reciprocal space: the rectangle marks the region of the Brillouin zone which can be detected simultaneously for orientation of the surface normal being parallel to the analyzer lens axis. Azimuthal rotation of the sample allows for the selection of different cuts through the surface Brillouin zone.

work were 42 meV and 0.4° , respectively. To reduce the effects of stray fields and enlarge the angular range that can be detected simultaneously, the sample was biased by a voltage of -10 V with respect to the analyzer entrance. In the case of a homogeneous and linearly increasing electrical field between sample and analyzer, the parallel momenta $\hbar k_{\parallel}$ of the photoelectrons are conserved in spite of the acceleration [23]. For the experimental setup used in the present study the effect of a sample bias on the ARPES signal was checked for voltages of up to -10 V in a two-photon photoemission experiment from the $n = 1$ image potential state of a Cu(100) surface [24].

The ultrahigh vacuum chamber is, furthermore, equipped with standard surface preparation and analysis units, including sputtering, heating, and cooling facilities, a three-cell organic evaporator (OVD-3; Ventiotec), a microquartz balance, and a LEED/Auger system with a dual-microchannel plate detector (BDL600IR MCP2; OCI Vacuum).

For experiments a Ag(111) single crystal (MaTecK) was prepared by several cycles of argon-ion sputtering (with an energy of 500 eV at incident angles of $\pm 65^\circ$ for 15 min, respectively) and annealing to 800 K [25] until sharp LEED spots and a narrow photoemission bandwidth (< 50 meV) of the Ag(111) Shockley surface state were observed [26].

SnPc molecules were deposited on the Ag(111) surface at room temperature at a rate of 0.1 ML per minute and at a base pressure below 2×10^{-10} mbar. The evaporation rate was checked with a microquartz balance before and after deposition. A coverage of 0.9 ML was achieved by successive evaporation and quantitative analysis of the LEED pattern under consideration of reference data [16]. This procedure allows the reproducible preparation of a SnPc coverage with an accuracy of $\approx \pm 0.05$ ML. For the preparation of a coverage of 1.0 ML, a film thickness of > 1.0 ML was evaporated, followed by the removal of the excess coverage by annealing of the sample to 523 K for 10 min [27].

III. RESULTS AND DISCUSSION

A. Pristine Ag(111)

Figure 3 shows an ARPES intensity map recorded at a photon energy of 5.9 eV. Two bands are visible in the photoemission spectrum, which we associate with the Ag(111)

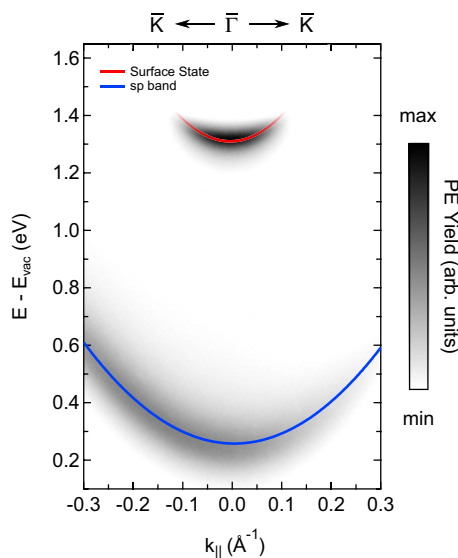


FIG. 3. ARPES intensity map of pristine Ag(111) recorded at 293 K in the $\bar{K}-\bar{\Gamma}-\bar{K}$ direction using p -polarized laser light ($h\nu = 5.9$ eV). Final-state energies are given with respect to the vacuum level E_{vac} . Positive momenta correspond to electrons emitted towards the incident laser. Red and blue lines are fits to the dispersion of the Shockley surface state and the sp intraband transition (primary Mahan cone L_0), respectively.

Shockley surface state [28] and a resonant sp -band transition [14,15], respectively. In the notation introduced below we refer the sp -band transition to the primary Mahan cone L_0 . A fit to the dispersion of the surface state yields an effective mass of $m_{\text{eff,ss}} = 0.45m_e$ with m_e being the mass of the electron. This value is in very good agreement with reference literature [26,28].

The effective mass of the sp -band transition is $m_{\text{eff,sp}} = 1m_e$ in agreement with prior work [29]. It implies a reasonable description of this spectral signature within a nearly free electron approximation which is used below for the quantitative description of spectral modifications observed for adsorption of SnPc molecules.

The asymmetry in the angular photoemission distribution of the sp -band transition originates from the broken symmetry in the detection geometry with respect to the incident laser beam and the electron emission angles captured by the analyzer [see Fig. 2(c)]: the photocurrent scales with the scalar product of the vector potential \vec{A} of the incident laser and the photoelectron momentum $\hbar\vec{k}$ [30,31]; i.e., a decrease in the photoemission yield is expected for electron emission towards the incident laser beam (positive momentum values), in agreement with our data.

B. 1.0ML SnPc on Ag(111)

Figures 4(a) and 4(c) show ARPES intensity maps for 1.0 ML SnPc/Ag(111) recorded with s -polarized light along $\bar{K}-\bar{\Gamma}-\bar{K}$ and $\bar{M}(L)-\bar{\Gamma}-\bar{M}(X)$, respectively. The adsorption of the SnPc overlayer results in the formation of a multitude of bands in the spectra. Due to their strong dispersion we exclude the possibility that molecular orbitals of SnPc are the origin of these bands. Furthermore, the energies of the bands do not match the binding energies of molecular orbitals for SnPc on Ag(111) as reported in STS [32,33] and PES [34,35] studies. Instead, we show in the following that these bands correspond to secondary Mahan cones resulting from umklapp-scattering processes acting on primary Mahan cones of the Ag(111) substrate in the presence of the adsorbed SnPc superstructure.

The formation of primary Mahan cones in a photoemission process can most intuitively be understood starting from the band structure model of a solid in the empty lattice approximation in one dimension [5,10] (details are also given in [36]). Here, a direct optical transition at a given photon energy $h\nu$ from an initial state with momentum \vec{k}_i and energy E_i to a final state with energy $E_f = E_i + h\nu$ and momentum \vec{k}_f is only possible if the lattice can deliver the missing momentum in terms of a reciprocal lattice vector $\vec{G} = \vec{k}_f - \vec{k}_i$. This model can easily be extended to three dimensions: In this case, possible initial states at energy E_i form isoenergy surfaces in momentum space which, in a nearly free electron approximation, are spheres with a radius $\sqrt{2m_{\text{eff}}E}/\hbar$ that are centered with respect to the reciprocal lattice points. Possible direct optical transitions at a given photon energy $h\nu$ correspond here to rings where the initial-state spheres shifted by a reciprocal lattice vector \vec{G} intersect the final-state sphere centered at Γ . The final states $E_f(\vec{k}_f)$ that are populated from the energy continuum of initial states form a so-called primary Mahan cone around the reciprocal lattice vector \vec{G} . The dispersion of the Mahan cone as probed in a photoemission

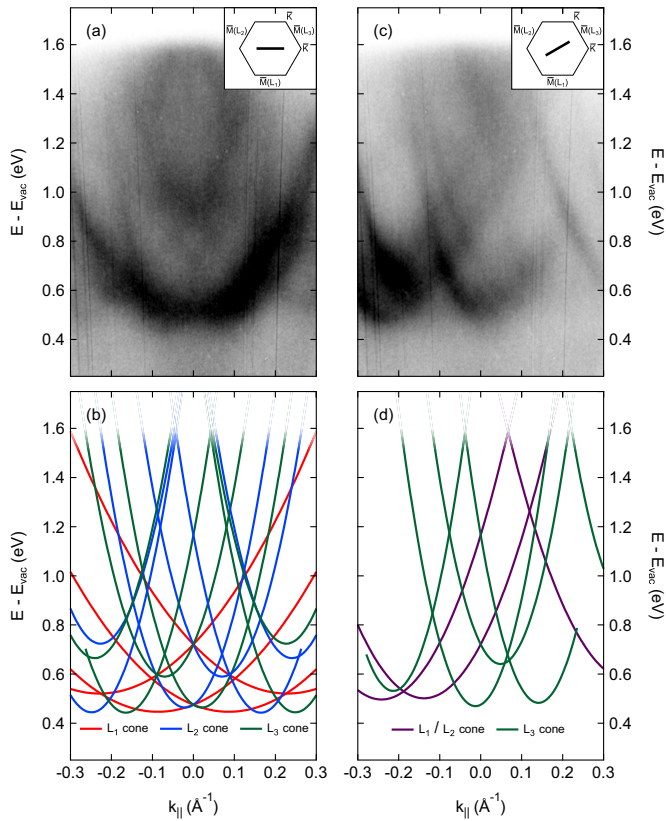


FIG. 4. Mahan cone formation for 1.0 ML SnPc on Ag(111). (a) ARPES intensity map and (b) calculated secondary Mahan cones in the $\bar{K}-\bar{\Gamma}-\bar{K}$ direction (see inset); cones originating from the three off-normal $\Gamma-L$ directions are depicted in different colors. (c) ARPES intensity map and (d) calculated secondary Mahan cones in the $\bar{M}(L)-\bar{\Gamma}-\bar{M}(X)$ direction; ARPES data were recorded at 293 K using s -polarized laser light ($h\nu = 5.9$ eV). Final-state energies are given with respect to the vacuum level E_{vac} . Note that the different maximum energies in comparison to pristine Ag(111) in Fig. 3 result from a change in the work function of about 250 meV caused by the adsorption of SnPc.

experiment is given by $E_f(\vec{k}_f)$ and is in the nearly free electron approximation parabolic. A prominent example of a primary Mahan cone is the resonant sp -band transition of Ag(111) mentioned above. The ARPES intensity distribution in Fig. 3 corresponds to a cut through the Mahan cone perpendicular to the relevant lattice vector \vec{G} pointing in the $\Gamma-L$ direction. As for a photon energy of $h\nu = 5.9$ eV electron states far inside the bulk Brillouin zone of silver are probed, the mapped dispersion can be well described by a free electron parabola.

In the presence of a two-dimensional surface superstructure, the photoelectrons of a primary Mahan cone can take up additional momentum via surface umklapp processes, resulting in the formation of secondary Mahan cones. While the parallel momentum can be changed by a reciprocal vector $\vec{G}_{S\parallel}$ of the surface superstructure, the perpendicular momentum must at the same time be altered to ensure energy conservation. This can result in the photoemission of electrons that would not have enough energy to overcome the surface potential barrier without the scattering at the surface. From a primary Mahan cone a multitude of secondary cones can be formed, as the

superstructure can contribute different lattice vectors $\vec{G}_{S\parallel}$ to the scattering process.

For interpretation of the ARPES data in Figs. 4(a) and 4(c) the energy-momentum distribution of the detected photoelectrons is simulated for SnPc on Ag(111) under consideration of Mahan processes using a model presented in Ref. [10]. Details of the simulations are discussed in [36]. Four primary Mahan cones must be included in the simulation: the cone centered along the $[111]$ surface normal direction (L_0 cone) and—for the calculation of secondary cones—three off-normal primary cones arising from the equivalent $\Gamma-L$ directions $[1\bar{1}\bar{1}]$, $[\bar{1}\bar{1}1]$, and $[\bar{1}1\bar{1}]$ [denoted L_1 , L_2 , and L_3 cones, corresponding to the three $\bar{M}(L)$ points indicated in the inset in Fig. 4(a)]. The reciprocal lattice vectors \vec{G}_{111} of the equivalent $\Gamma-L$ directions are the shortest to be found in a face-centered cubic structure ($|\vec{G}_{111}| = 2 \cdot \sqrt{3} \cdot \pi/a$, with a being the lattice constant). It turns out that all secondary cones arising from primary cones centered along larger reciprocal lattice vectors (for example, in the $\Gamma-X$ direction with $|\vec{G}_{100}| = 4 \cdot \pi/a$) exhibit kinetic energies that are not accessible with the used photon energy of 5.9 eV. The superstructure of 1.0 ML SnPc on Ag(111) yields six adsorption domains. Each of them is spanned by two reciprocal basic vectors which can be calculated from the superstructure matrices given in Ref. [16]. Any vector $\vec{G}_{S\parallel}$ causing the formation of a secondary Mahan cone can be represented by any linear combination of reciprocal basic vectors of the same domain. As the Brillouin zone of the SnPc superstructure is small compared to that of the silver substrate, the resulting secondary cones lie very close to each other. Due to the symmetry properties of the substrate and superstructure, some of the secondary cones turn out to be equivalent: The twofold mirror symmetry of the substrate reduces the effective number of differing superstructure domains by a factor of 2. Additionally, the threefold rotational symmetry of the substrate affects the Mahan cone spectra, as discussed later.

To account for the resonant sp transition of pristine Ag(111), we simulated the primary L_0 Mahan cone using a photon energy of $h\nu = 5.9$ eV, a lattice constant of $a_{\text{Ag}} = 4.085$ \AA [37], and an electron effective mass of $m_{\text{eff},sp} = 1m_e$. The inner potential V_0 , which is defined as the free electron band minimum E_0 with respect to the vacuum energy E_{vac} , is used as a free parameter in the Mahan cone calculation. A fit to the data results in an inner potential of $V_0 = 9.78$ eV, in good agreement with other work [38,39]. This model as well as the nearly free electron approximation presented before result in the same parabolic band dispersion and match the experimental data very well (see blue line in Fig. 3).

Due to matrix element effects in the photoemission process, the primary L_0 cone dominates the ARPES spectrum for excitation with p -polarized light [14] and strongly conceals secondary cones. For comparison with the simulations the ARPES intensity maps of the SnPc-covered Ag(111) surface shown in Figs. 4(a) and 4(c) were recorded with s -polarized light. In this case, the primary L_0 cone and the resultant secondary cones are not visible and can be omitted in the simulation. As the typical SnPc domain size (≈ 500 \AA ² [16]) is very small compared to the laser spot size at the sample surface ($\approx 4 \times 10^{-2}$ mm²), all six adsorption domains contribute to the ARPES signal and must be included in the calculation. Cuts of

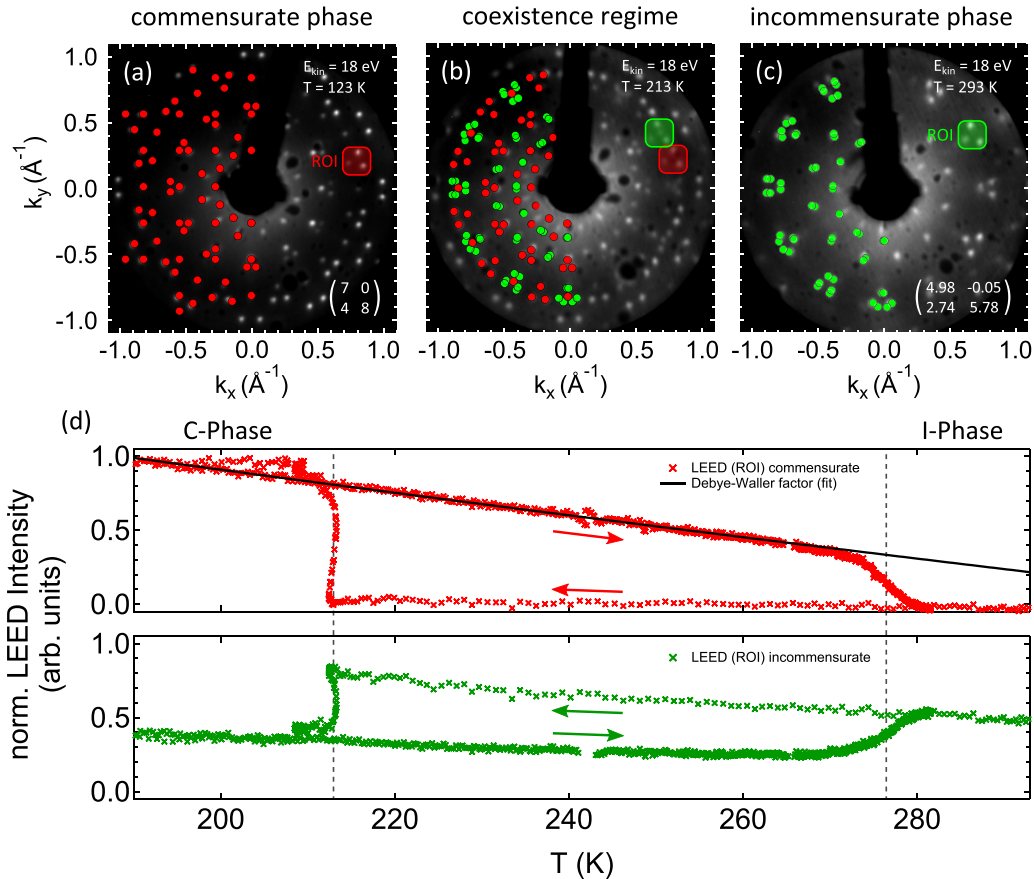


FIG. 5. Structural phase transition of 0.9 ML SnPc on Ag(111) investigated with LEED. (a)–(c) LEED images recorded at 123 K (commensurate phase), 213 K (at the phase transition), and 293 K (incommensurate phase); red and green points represent calculated LEED spots of the commensurate and incommensurate phase, respectively, according to the indicated superstructure matrices taken from [16]. Data were recorded at incident electron energy $E_{\text{kin}} = 18$ eV. LEED images in (a)–(c) are corrected for an azimuthal sample rotation observed during the temperature scan. (d) Temperature dependence of LEED spot intensities representing the commensurate phase (red \times 's) and incommensurate phase (green \times 's). Representative spot groups selected for this analysis are correspondingly labeled ROI in (a)–(c). Intensity curves in (d) result from averaging over all equivalent spot groups. Data are referenced with respect to the minimum intensity level of the commensurate phase (zero level) and the maximum intensity observed in this phase at $T = 170$ K. Arrows indicate the direction of the respective temperature scan. The black line is the fit of a Debye-Waller factor to the data in the commensurate phase and during sample heat-up.

the simulation results along the $\bar{K}-\bar{\Gamma}-\bar{K}$ and $\bar{M}(X)-\bar{\Gamma}-\bar{M}(L)$ directions are shown for comparison with the ARPES data in Figs. 4(b) and 4(d), respectively. For clarity, only bands which can clearly be identified in the experimental data are shown. Furthermore, the calculated cones are color-coded with respect to the primary cone (L_1 , L_2 , or L_3) they originate from. The comparison with the experimental data show that all three $\bar{\Gamma}-L$ directions contribute to the photoemission signal.

The ARPES intensity distributions as well as the calculated Mahan cone cuts exhibit different symmetries with respect to $\bar{\Gamma}$ depending on the probed direction, $\bar{K}-\bar{\Gamma}-\bar{K}$ or $\bar{M}(X)-\bar{\Gamma}-\bar{M}(L)$. This difference is caused by the threefold rotational symmetry of the Ag(111) substrate: whereas the six \bar{K} points of the Ag(111) surface are equivalent [see Fig. 2(c)], the \bar{M} points can result from a surface projection of the L or the X point of the three-dimensional Brillouin zone. Hence, only the pattern formed by the Mahan cone cuts along $\bar{\Gamma}-\bar{K}$ is symmetric with respect to $\bar{\Gamma}$ [Figs. 4(a) and 4(b)]. Furthermore, the detection cut in momentum space as indicated in the inset in Fig. 4(a) implies a mirror symmetry of L_2 and L_3

secondary cones with respect to each other, in agreement with the results of experiment and simulation. Along $\bar{\Gamma}-\bar{M}$, the symmetry of the Mahan cone cuts with respect to $\bar{\Gamma}$ is lost [Figs. 4(c) and 4(d)]. In this case, one expects the projections along L_1 and L_2 to be identical, suggesting that the secondary cones from these two primary cones lie on top of each other. Once again, experiment and simulation confirm this conclusion.

Based on the qualitative agreement, the structures can be clearly identified as secondary Mahan cones. However, there are some quantitative deviations between experimental data and simulations. We attribute these to the simplified description within the free electron approximation. Details are discussed in [36].

C. 0.9 ML SnPc on Ag(111)

At a coverage of 0.9 ML the room-temperature phase of the SnPc overlayer exhibits an incommensurate superstructure. Upon cooling the sample below 220 K the system undergoes

a structural transition into a commensurate phase, which is not observed for a coverage of 1.0 ML. The phase transition is accompanied by a change in the molecular interaction from repulsive to attractive, resulting in the formation of islands with a local coverage of 0.94 ML [16]. The transition from incommensurate to commensurate phase can be directly observed as distinct changes in the LEED pattern and, as shown below, also in changes in the Mahan cone pattern mapped in the photoemission experiment.

LEED results from a temperature scan of 0.9 ML SnPc on Ag(111) are summarized in Fig. 5. Starting at room temperature, the sample was cooled down below 180 K and then heated up again to room temperature. Figures 5(a)–5(c) show LEED images recorded in the commensurate phase of the SnPc overlayer [123 K; Fig. 5(a)], at/near the transition temperature [213 K; Fig. 5(b)], and in the incommensurate phase [293 K; Fig. 5(c)]. For comparison, simulated LEED patterns under consideration of the corresponding superstructure matrices [16] are included in the images and show a very good agreement with the experimental data. This becomes particularly evident in the LEED image recorded near the transition temperature where both superstructures are superimposed.

Figure 5(d) shows LEED spot intensities as a function of temperature as observed for incommensurate (green x's) and commensurate phase (red x's). For the quantitative analysis equivalent spot groups in the LEED patterns characteristic for the respective phases were selected. The red and green regions of interest (ROI) in Figs. 5(a) and 5(c), respectively, show representatives of these spot groups. In the coexistence regime shown in Fig. 5(b) the ROIs of both phases are indicated. The temperature-dependent intensities in Fig. 5(d), finally, result from an averaging over all equivalent spot groups present in the LEED pattern. Both traces show a distinct hysteresis indicative of a first-order phase transition as expected for a structural phase transition: upon cooling the phase transition occurs at 213 K; upon heating it occurs at 275 K. At the same time, the slopes of the intensity traces at the phase transitions clearly differ, with the slopes during cooldown being significantly steeper.

The temperature dependence of the LEED spot intensities within a structural phase arises from thermal motion of the atoms in the adsorbate layer. For a quantitative analysis we assumed that the temperature dependence follows the Debye-Waller factor $B = \exp(-\frac{\Delta k^2}{\Theta_D} \cdot T)$, with Δk being the momentum transfer in the diffraction process and Θ_D the Debye temperature of the adsorbed SnPc layer. Due to multiple phonon scattering processes contributing to the LEED signal at low electron kinetic energies, such an analysis has only limited quantitative significance [40]. However, as we show below, it allows for a direct comparison of the LEED data with the photoemission results. The solid black line in Fig. 5(d) is a fit of the Debye-Waller factor to the experimental data with $\Delta k = 4 \cdot G_{S\parallel}$ as evaluated from the LEED data, yielding a value of $\Theta_D \approx 8$ K. In contrast to the commensurate phase, the Debye-Waller factor of the incommensurate phase cannot be determined from the LEED data for two reasons. On the one hand, there is an extra spot of the commensurate phase located within the ROI of the incommensurate phase. This additional spot is also the reason for the slope during the cooldown being different from 0. On the other hand, the six spots within the

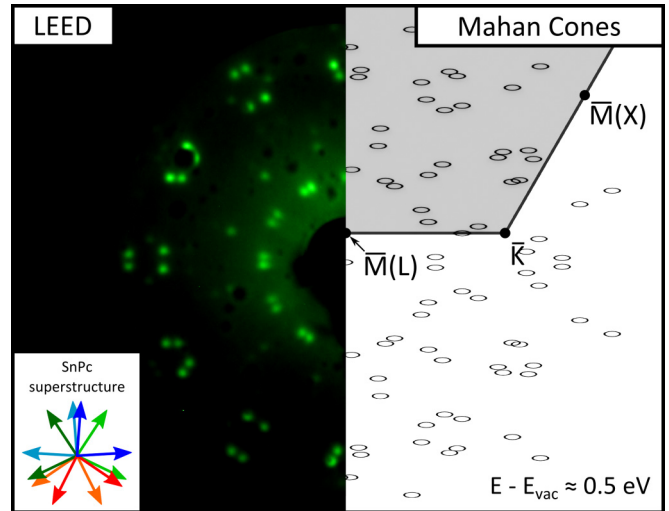


FIG. 6. Correlation between LEED pattern and secondary Mahan cone pattern: LEED image of the incommensurate phase (left) in comparison to a calculated secondary Mahan cone pattern formed from equienergy surfaces (right). An intermediate energy value of $E - E_{\text{vac}} = 0.5$ eV was chosen for calculations of the equienergy surfaces, as the results at this energy illustrate, at the same time, the correspondence between Mahan cone signal and LEED pattern as well as the conelike character of the Mahan pattern. The gray shaded area indicates the position of the surface-projected first Brillouin zone with respect to the Mahan cone pattern. $\bar{\Gamma}$ is located outside the image centered slightly above the top border. Inset: Orientations of the six adsorption domains.

ROI belong to two different orders of diffraction (second and third orders); i.e., Δk is not uniquely defined.

As the formation of the Mahan cones arises from elastic scattering of photoemitted electrons by the SnPc superstructure, information equivalent to the LEED results should also be encoded in temperature-dependent ARPES spectra. The equivalence of LEED and Mahan-cone spectroscopy is illustrated in Fig. 6 for the incommensurate phase of SnPc/Ag(111). The LEED pattern coincides with the (calculated) equienergy surfaces of the secondary Mahan cones at one of the three $\bar{M}(L)$ points. Similarly to the differences in the LEED patterns for the incommensurate and the commensurate phase we therefore expect also significant changes in the Mahan cone spectra as the system undergoes the phase transition.

ARPES intensity maps of 0.9 ML SnPc/Ag(111) recorded in the commensurate phase (115 K) and in the incommensurate phase (293 K) are shown in Figs. 7(a) and 7(b). In contrast to Figs. 4(a) and 4(c) for these experiments we used p -polarized light in order to enhance the signal from the primary L_0 cone. This reference was utilized to compensate for temperature-dependent shifts in the angular distribution of the photoemission spectra. The shifts arise from a rotation of the sample, which is most likely caused by thermal strain acting on the sample manipulator during cooldown and heat-up. The different polarization is responsible for the significantly reduced number of visible Mahan cones in the incommensurate phase compared to that in the spectra for 1.0 ML SnPc/Ag(111) in Fig. 4. The structural changes going along with the phase transition can clearly be discerned in the photoemission data. Besides the

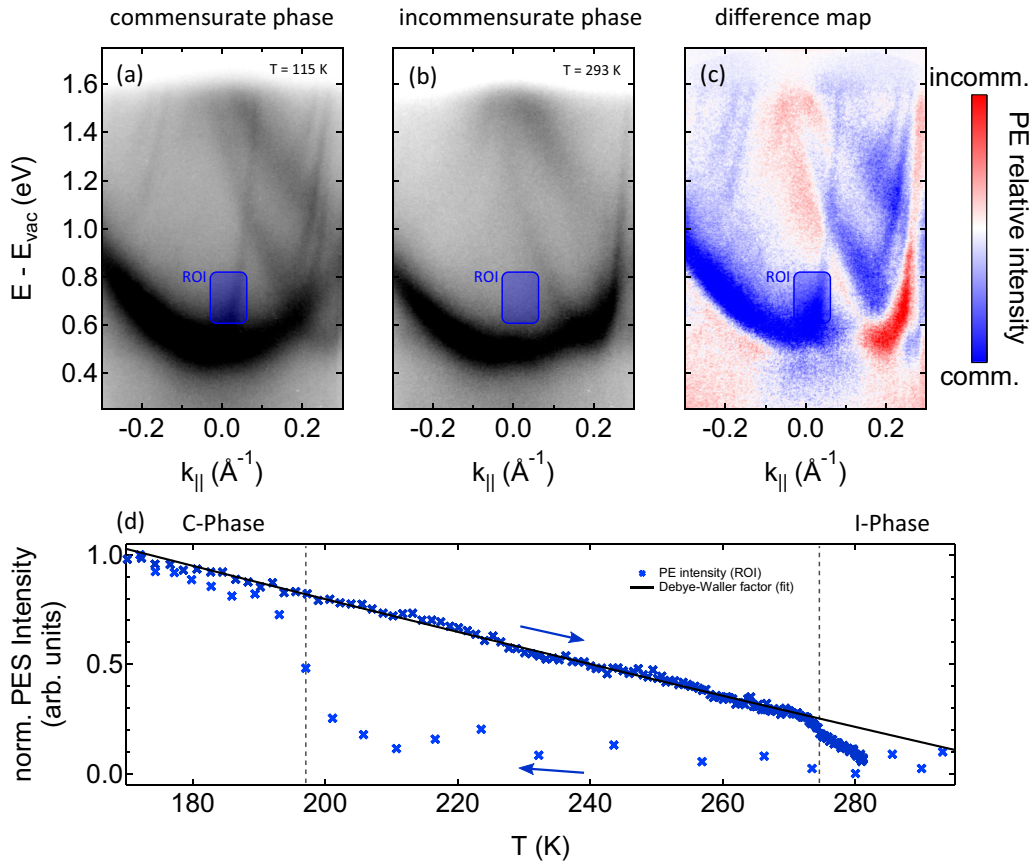


FIG. 7. Structural phase transition of 0.9 ML SnPc on Ag(111) investigated with photoemission along $\bar{M}(X)-\bar{\Gamma}-\bar{M}(L)$. Selected ARPES intensity maps of (a) the commensurate (115 K) and (b) the incommensurate (293 K) phases. (c) Difference intensity map generated from (a) and (b) illustrating the spectral changes going along with the phase transition. (d) Photoemission intensity as a function of the temperature from the ROI highlighted in (a)–(c). The region covers a secondary Mahan cone which is only visible in the commensurate phase. Arrows indicate the direction of the respective temperature scan. Data are referenced with respect to the minimum intensity level (zero level) and the maximum intensity observed at $T = 170$ K.

energy-momentum shifts of the main features, also new Mahan cone bands appear as the commensurate phase is formed. These changes are best seen in a difference intensity map generated from the two spectra as shown in Fig. 7(c). Here, red (blue) regions indicate a decrease (increase) in the photoemission intensity as the SnPc overlayer undergoes the phase transition from the incommensurate to the commensurate phase.

The result of a quantitative analysis of the temperature dependence of the photoemission intensity maps is shown in Fig. 7(d). The graph displays the integral photoemission signal as a function of the sample temperature from the selected ROI shown in Fig. 7(a) covering a Mahan cone band visible only in the commensurate phase. The result of this analysis is in quite good agreement with the temperature-dependent data from the LEED spot analysis presented in Fig. 5(d). The ARPES data qualitatively reproduce hysteresis loop and transition temperatures. We associate the difference in the transition temperature between LEED and ARPES data during cooldown with slight differences in the actual SnPc coverage due to the experimental limitations in the reproducible preparation of a sample coverage. The broad transition regime observed for the ARPES data during cooldown results from the high cooling rates (≈ 1 K/s) in combination with the limited time resolution available in the ARPES experiments, which require acquisition

times of ≈ 30 s. High-quality LEED images, in contrast, could be recorded with an exposure time of ≈ 1 s. Furthermore, the Debye-Waller analysis matches the results of the LEED scan very well: For the fit to the ARPES data the Debye temperature was fixed to a value $\Theta_D = 8$ K as determined from the analysis of the LEED data and the momentum transfer Δk was set as the free fit parameter. The fit yields $\Delta k = 4 \cdot G_{S\parallel}$, i.e., in the experiment a secondary Mahan cone of fourth order is probed, in agreement with the result of the simulations.

IV. OUTLOOK AND CONCLUSION

Summing up our findings, the conspicuous band structure observed in the ARPES data on SnPc/Ag(111) can be associated with secondary Mahan cones resulting from the diffraction of electrons photoexcited in the silver substrate by the adsorbate superstructure. Furthermore, the analysis of the ARPES data yields results quantitatively similar to those obtained in a LEED study, potentially providing detailed insights into the structural properties of the adsorbate layer as probed in reciprocal space. Notably and in contrast to the presented LEED experiments, the diffraction pattern observed in ARPES is formed from the diffraction of electron pulses generated by femtosecond laser pulses. This particular detail of the

present experiment opens up new and fascinating perspectives for the study of structural dynamics in adsorbate-surface systems. Time-resolved electron diffraction using pulsed electron sources has emerged over the last decade as a key instrument in studying ultrafast structural dynamics in solids and their surfaces [41]. Different approaches have been presented in the past, including time-resolved electron diffraction operated in transmission [42], reflection [43], and LEED [44] geometry. One of the main problems in the operation of these types of experiments, substantially limiting the achievable temporal resolution, arises from the repulsive Coulomb interaction among the electrons, resulting in the temporal spreading of an electron pulse as it propagates from the electron source to the sample. Strategies to compensate for or overcome this problem include the use of relativistic electrons [45], the implementation of electron pulse compression units [46], and an effective reduction of the distance between electron source and sample [47]. The experimental configuration available in the present study is the ultimate limit of what can be achieved for the latter scenario. The electron source, i.e., the silver substrate, is placed in the direct vicinity of the structure to be probed, i.e., at an atomic distance from the adsorbate overlayer. Hence, the electron pulse as it is diffracted by the adsorbate superstructure is virtually not spread by Coulomb interaction and is therefore still expected to carry the temporal profile as imprinted by the excitation laser pulse. A cross-correlation measurement performed on a graphite sample using the time-resolved ARPES configuration of the experiment shown in Fig. 2(a) yields a pulse width of 70 fs (FWHM) for the 210-nm laser pulse, providing an estimate of the temporal width of the diffracted electron pulse. Operated in a pump-probe configuration we therefore envision the realization of time-resolved electron diffraction experiments routinely providing a sub-100-fs temporal resolution. Additionally, the capabilities of time-resolved ARPES will provide insights not only into ultrafast structural dynamics but also, at the same time, into dynamics associated with electronic excitations generated upon absorption of the pump pulse [48,49]. For SnPc/Ag(111), the analysis of transient changes in the Mahan cone signal probed in such an experiment will allow, in the first instance, monitoring in real time of the temperature rise of the adsorbate layer in response to optical excitation. The time scale for this process will critically depend on how the adsorbate layer

couples to the substrate. A fast response, on the time scale of a few hundred femtoseconds, is characteristic for an electronic-driven process [50,51]. Such a scenario could involve, for instance, resonant electron transfer processes where a hot carrier population generated in the substrate by absorption of the pump pulse couples to electronic states of the adsorbate. Also, the dynamics of these initiating electronic processes are potentially observable in the time-resolved ARPES data [49]. For a phonon-driven heat-up of the adsorbate layer we expect, in contrast, characteristic response times in the picosecond regime [52]. At sufficiently high pump fluences it might even become possible to monitor the dynamics associated with a laser-induced structural phase transition between commensurate and incommensurate phase provided that excitation conditions under which the adsorbate layer is not irreversibly destroyed can be realized. In a preliminary experiment, we illuminated the SnPc/Ag(111) sample for 2 h with 60-fs pump pulses (800 nm) at a fluence of $\approx 1 \text{ mJ cm}^{-2}$, a value which is of the order of what is typically used for studies of transient structural phase transitions in bulk solids [42]. Inspection of the sample with ARPES and LEED before and after illumination showed no indication of a permanent structural destruction of the adsorbate layer.

In the present example, primary Mahan cone formation in silver acts as a characteristic signature required for distinct spectral discrimination of the diffraction pattern, potentially limiting the proposed approach to a restricted number of systems. However, the observation of primary Mahan cones in low-energy photoemission has been reported for other substrate systems [5,53]. Furthermore, we expect that also other types of valence electronic spectral signatures can give rise to a diffraction pattern from a surface superstructure. Notably, also, other time-resolved electron diffraction techniques are subject to constraints limiting their application to certain sample systems and problems.

ACKNOWLEDGMENTS

We thank Mirko Cinchetti (University of Dortmund) for helpful discussion. This work was funded by the German Research Foundation (DFG) through the Collaborative Research Center 677 Function by Switching.

S.J. and P.H. contributed equally to this work.

-
- [1] J. Anderson and G. J. Lapeyre, *Phys. Rev. Lett.* **36**, 376 (1976).
 - [2] D. Westphal and A. Goldmann, *Surface Sci.* **126**, 253 (1983).
 - [3] O. Rader and A. M. Shikin, *Phys. Rev. Lett.* **93**, 256802 (2004).
 - [4] F. C. Bocquet, L. Giovanelli, P. Amsalem, L. Petaccia, D. Topwal, S. Gorovikov, M. Abel, N. Koch, L. Porte, A. Goldoni, and J. M. Themlin, *Phys. Rev. B* **84**, 241407(R) (2011).
 - [5] A. Winkelmann, A. A. Únal, C. Tusche, M. Ellguth, C. T. Chiang, and J. Kirschner, *New J. Phys.* **14**, 083027 (2012).
 - [6] G. Paolucci, K. Prince, B. Hayden, P. Davie, and A. Bradshaw, *Solid State Commun.* **52**, 937 (1984).
 - [7] K. Desinger, W. Altmann, and V. Dose, *Surface Sci.* **201**, L491 (1988).
 - [8] C. G. Larsson, J. Paul, and L. Walldén, *Phys. Scripta* **T4**, 44 (1983).
 - [9] S. Hüfner, *Photoelectron Spectroscopy*, 3rd ed. (Springer, Berlin, 1995).
 - [10] G. D. Mahan, *Phys. Rev. B* **2**, 4334 (1970).
 - [11] J. D. Koralek, J. F. Douglas, N. C. Plumb, J. D. Griffith, S. T. Cundiff, H. C. Kapteyn, M. M. Murnane, and D. Dessau, *Rev. Sci. Instrum.* **78**, 053905 (2007).
 - [12] Z. Yong, G.-L. Wang, C.-M. Li, Q.-J. Peng, D.-F. Cui, Z.-Y. Xu, X.-Y. Wang, Y. Zhu, C.-T. Chen, G.-D. Liu, X.-L. Dong, and X.-J. Zhou, *Chin. Phys. Lett.* **25**, 963 (2008).

- [13] T. Miller, W. E. McMahon, and T.-C. Chiang, *Phys. Rev. Lett.* **77**, 1167 (1996).
- [14] S. Pawlik, R. Burgermeister, M. Bauer, and M. Aeschlimann, *Surface Sci.* **402**, 556 (1998).
- [15] A. Winkelmann, V. Sametoglu, J. Zhao, A. Kubo, and H. Petek, *Phys. Rev. B* **76**, 195428 (2007).
- [16] C. Stadler, S. Hansen, I. Kröger, C. Kumpf, and E. Umbach, *Nat. Phys.* **5**, 153 (2009).
- [17] P. Day, Z. Wang, and R. Pachter, *J. Mol. Struct. THEOCHEM* **455**, 33 (1998).
- [18] M. Lackinger and M. Hietschold, *Surface Sci.* **520**, L619 (2002).
- [19] C. Stadler, S. Hansen, F. Pollinger, C. Kumpf, E. Umbach, T. L. Lee, and J. Zegenhagen, *Phys. Rev. B* **74**, 035404 (2006).
- [20] W. Yongfeng, J. Kröger, R. Berndt, and W. A. Hofer, *J. Am. Chem. Soc.* **131**, 3639 (2009).
- [21] B. J. Siwick, J. R. Dwyer, R. E. Jordan, and R. J. D. Miller, *J. Appl. Phys.* **92**, 1643 (2002).
- [22] Z. Tao, H. Zhang, P. M. Duxbury, M. Berz, and C. Y. Ruan, *J. Appl. Phys.* **111**, 044316 (2012).
- [23] M. Hengsberger, F. Baumberger, H. J. Neff, T. Greber, and J. Osterwalder, *Phys. Rev. B* **77**, 085425 (2008).
- [24] See Supplemental Material at <http://link.aps.org/supplemental/10.1103/PhysRevB.97.125413> for ARPES data of Cu(100) recorded at different sample bias voltages (Sec. II).
- [25] R. Musket, W. McLean, C. Colmenares, D. Makowiecki, and W. Siekhaus, *Appl. Surface Sci.* **10**, 143 (1982).
- [26] R. Paniago, R. Matzdorf, G. Meister, and A. Goldmann, *Surface Sci.* **336**, 113 (1995).
- [27] R. A. J. Woolley, C. P. Martin, G. Miller, V. R. Dhanak, and P. J. Moriarty, *Surface Sci.* **601**, 1231 (2007).
- [28] F. Reinert, G. Nicolay, S. Schmidt, D. Ehm, and S. Hüfner, *Phys. Rev. B* **63**, 115415 (2001).
- [29] A. Samsavar, T. Miller, and T. C. Chiang, *J. Phys. Condens. Matter* **2**, 1141 (1990).
- [30] P. Puschnig and D. Lüftner, *J. Electron Spectrosc. Relat. Phenom.* **200**, 193 (2015).
- [31] S. Hüfner, R. Claessen, F. Reinert, T. Straub, V. Strocov, and P. Steiner, *J. Electron Spectrosc. Relat. Phenom.* **100**, 191 (1999).
- [32] M. Toader and M. Hietschold, *J. Phys. Chem. C* **115**, 3099 (2011).
- [33] Y. Wang, J. Kröger, R. Berndt, and W. Hofer, *Angew. Chem. Int. Ed.* **48**, 1261 (2009).
- [34] M. Häming, C. Scheuermann, A. Schöll, F. Reinert, and E. Umbach, *J. Electron Spectrosc. Relat. Phenom.* **174**, 59 (2009).
- [35] M. Häming, M. Greif, C. Sauer, A. Schöll, and F. Reinert, *Phys. Rev. B* **82**, 235432 (2010).
- [36] See Supplemental Material at <http://link.aps.org/supplemental/10.1103/PhysRevB.97.125413> for a detailed description of the Mahan cone simulations (Sec. I).
- [37] L. G. Liu and W. A. Bassett, *J. Appl. Phys.* **44**, 1475 (1973).
- [38] H. Wern, R. Courths, G. Leschik, and S. Hüfner, *Z. Phys. B Condens. Matter* **60**, 293 (1985).
- [39] S. C. Wu, H. Li, J. Sokolov, J. Quinn, Y. S. Li, and F. Jona, *J. Phys. Condens. Matter* **1**, 7471 (1989).
- [40] M. A. Van Hove, W. H. Weinberg, and C.-M. Chan, *Low-Energy Electron Diffraction—Experiment, Theory and Surface Structure Determination* (Springer, Berlin, 1986).
- [41] G. Sciaini and R. J. D. Miller, *Rep. Prog. Phys.* **74**, 096101 (2011).
- [42] M. Eichberger, H. Schäfer, M. Krumova, M. Beyer, J. Demsar, H. Berger, G. Moriena, G. Sciaini, and R. J. D. Miller, *Nature* **468**, 799 (2010).
- [43] T. Frigge, B. Hafke, T. Witte, B. Krenzer, C. Streubühr, A. Samad Syed, V. Mikšić Trontl, I. Avigo, P. Zhou, M. Ligges, D. von der Linde, U. Bovensiepen, M. Horn-von Hoegen, S. Wippermann, A. Lücke, S. Sanna, U. Gerstmann, and W. G. Schmidt, *Nature* **544**, 207 (2017).
- [44] M. Gulde, S. Schweda, G. Storeck, M. Maiti, H. K. Yu, A. M. Wodtke, S. Schafer, and C. Ropers, *Science* **345**, 200 (2014).
- [45] J. B. Hastings, F. M. Rudakov, D. H. Dowell, J. F. Schmerge, J. Cardoza, J. Castro, S. Giermann, H. Loos, and P. M. Weber, *Appl. Phys. Lett.* **89**, 184109 (2006).
- [46] R. P. Chatelain, V. R. Morrison, C. Godbout, and B. J. Siwick, *Appl. Phys. Lett.* **101**, 081901 (2015).
- [47] G. Storeck, S. Vogelgesang, M. Siviš, S. Schäfer, and C. Ropers, *Struct. Dynam.* **4**, 044024 (2017).
- [48] W. S. Fann, R. Storz, H. W. Tom, and J. K. Bokor, *Phys. Rev. B* **46**, 13592 (1992).
- [49] U. Bovensiepen, *J. Phys. Condens. Matter* **19**, 083201 (2007).
- [50] F. Budde, T. F. Heinz, M. M. T. Loy, J. A. Misewich, F. De Rougemont, and H. Zacharias, *Phys. Rev. Lett.* **66**, 3024 (1991).
- [51] J. A. Prybyla, H. W. K. Tom, and G. D. Aumiller, *Phys. Rev. Lett.* **68**, 503 (1992).
- [52] T. A. Germer, J. C. Stephenson, E. J. Heilweil, and R. R. Cavanagh, *Phys. Rev. Lett.* **71**, 3327 (1993).
- [53] M. Traum and N. Smith, *Surface Sci.* **53**, 121 (1975).